Published in final edited form as:

Nat Biomed Eng. 2018 September ; 2(9): 666–674. doi:10.1038/s41551-018-0265-3.

Design and clinical validation of a point-of-care device for the diagnosis of lymphoma via contrast-enhanced microholography and machine learning

Hyungsoon Im[1,2,†], **Divya Pathania**[1,†], **Philip J. McFarland**[1], **Aliyah R. Sohani**[3], **Ismail Degani**[1,4], **Matthew Allen**[1], **Benjamin Coble**[1,5], **Aoife Kilcoyne**[1,2], **Seonki Hong**[1], **Lucas Rohrer**[1,6], **Jeremy S. Abramson**[7], **Scott Dryden-Peterson**[8,9,10], **Lioubov Fexon**[1], **Mikhail Pivovarov**[1,2], **Bruce Chabner**[7], **Hakho Lee**[1,2], **Cesar M. Castro**[1,7,*], and **Ralph Weissleder**[1,2,11,*]

[1]Center for Systems Biology, Massachusetts General Hospital, Boston, MA 02114, USA

[2]Department of Radiology, Massachusetts General Hospital, Boston, MA 02114, USA

[3]Department of Pathology, Massachusetts General Hospital, Boston, MA 02114, USA

[4]Department of Electrical Engineering and Computer Science, Massachusetts Institute of Technology, Cambridge, MA 02139, USA

[5]Department of Engineering and Management, Massachusetts Institute of Technology, Cambridge, MA 02139, USA

[6]Department of Health Sciences, Northeastern University, Boston, MA 02115, USA

[7]Massachusetts General Hospital Cancer Center, Boston, MA 02114, USA

[8]Botswana Harvard AIDS Institute, Gaborone, Botswana

[9]Division of Infectious Diseases, Brigham and Women's Hospital, Boston, MA 02115, USA

[10]Harvard T.H. Chan School of Public Health, Boston, MA 02115, USA

[11]Department of Systems Biology, Harvard Medical School, Boston, MA 02115, USA

Abstract

[*]R. Weissleder, MD, PhD (contact) or Cesar M. Castro, MD, Center for Systems Biology, Massachusetts General Hospital, 185 Cambridge St., CPZN 5206, Boston, MA, 02114, USA, 617-726-8226, rweissleder@mgh.harvard.edu; Castro.Cesar@mgh.harvard.edu.

[†]These authors contributed equally to the manuscript.

Author Contributions

H.I., H.L., C.M.C. and R.W. designed the study. H.I., I.D. and B.Coble designed and fabricated the CEM device. D.P., P.J.M. and H.I. designed and optimized experiments. H.I., D.P., P.J.M., H.I., S.H. and L.R., processed and analyzed samples. H.I., M.A., H.L., L.F. and M.P. established computational algorithms. R.W., A.K., A.R.S., J.S.A., B. Chabner and C.M.C conducted clinical trials. All authors reviewed the data. H.I. and R.W. wrote the paper, which was edited by all authors.

Competing interests

The authors declare that they have no competing interests.

The identification of patients with aggressive cancer who require immediate therapy is a health challenge in low-income and middle-income countries. Limited pathology resources, high healthcare costs and large-case loads call for the development of advanced standalone diagnostics. Here, we report and validate an automated, low-cost point-of-care device for the molecular diagnosis of aggressive lymphomas. The device uses contrast-enhanced microholography and a deep-learning algorithm to directly analyse percutaneously obtained fine-needle aspirates. We show the feasibility and high accuracy of the device in cells, as well as the prospective validation of the results in 40 patients clinically referred for image-guided aspiration of nodal mass lesions suspicious for lymphoma. Automated analysis of human samples with the portable device should allow for the accurate classification of patients with benign and malignant adenopathy.

Keywords

holography; deep learning; artificial intelligence; diagnostics; low-middle income countries; lymphoma; adenopathy; cancer

Modern oncology requires tissue-specific diagnoses prior to initiating appropriate therapies. This is commonly done by image-guided tumor biopsy, fine-needle aspirates (FNAs) or liquid biopsies where samples are processed by conventional immunohistochemistry, flow cytometry and/or genetic analysis. These procedures can be costly and time-consuming but nevertheless are essential in enabling precision medicine. In most developed countries, there are sufficient numbers of pathologists (typically >30 per million inhabitants) and related support structures so that sample processing, analysis and interpretation rarely encounter bottlenecks[1]. This picture is very different in low- and middle-income countries (LMICs) in Asia[1] and Africa; for example, several African countries report only 1 pathologist per million inhabitants[2]. Meanwhile, the global cancer burden is rising.

One of the specific health challenges in sub-Saharan Africa is the high prevalence of AIDS-related cancers (the “second wave of AIDS”)[3–5]. Some such cancers include very aggressive ones such as diffuse large B-cell lymphoma (DLBCL) and Burkitt’s lymphoma[6,7]. Due to limited resources, a considerable proportion of these cases evade comprehensive evaluation or are not appropriately classified. Diagnosis and care are hampered by lack of proper tissue specimens and diagnostic reagents, limited availability of trained pathologists/specialists and lack of access to care in rural settings. Although a good proportion of these cases are curable even in LMIC, windows of therapeutic opportunity are often missed[6,8]. As a result, there is a need for low-cost, fast, accurate detection technologies to expedite the diagnosis of lymphomas (and other prevalent cancers) in these environments.

Recent advances in digital image sensors and mobile platforms (e.g. smartphones, wearable electronics, microcomputers) have led to the development of digital point-of-care (POC) imaging systems that may address the lack or bottleneck of pathology specialists[9–20]. The diagnostic potential of these systems has been demonstrated by successful detection of various biological objects (e.g., tissues, cancer cells, sperm, parasites). Most of these targets, however, were identified via morphological features or a few defined markers. Detecting lymphoid cancers with portable imagers poses more technical challenges: i) clonal neoplastic lymphoid cells exist on a background of normal lymphocytes in blood; ii) target

cells are generally small, similar to the size of blood cells and iii) a diverse set of different surface markers need to be tested for disease classification. To address these challenges, clinical laboratories increasingly use flow cytometry despite its inherent limitations, such as high cost and under-diagnosing aggressive lymphomas due to lack of accurate size measurements and fragility of large cells[21–23]. Portable fluorescence microscopes could be used to profile molecular markers, but their limited field-of-view and need for expert interpretation make this approach less feasible[13,19,24].

Digital holography enables microscopic bright-field imaging with a large field-of-view over mm^2 and a high spatial resolution for single-cell analysis[10,12,25–27]. In prior research, we showed that molecular specificity can be obtained by labeling large epithelial cells with micrometer-sized beads that change the cells' holographic patterns[11,28]. For lymphoma diagnosis[28], however, the number of beads per cell is limited due to much smaller lymphoma cells, and the approach is incompatible with analyzing intracellular markers. To circumvent these drawbacks and to enable detection of intracellular proteins (e.g. Ki67), we hypothesized that small molecule chromogens would have to be used to modulate holographic patterns. Irrespective of the approach, there is currently no POC device for automated lymphoma diagnostics in LMIC.

Here, we developed an automated digital cellular analysis tool that enables analyses of specimens obtained from palpable mass lesions. Starting from microholography principles, we developed a contrast-enhanced micrography (CEM) that is simple, portable, robust, integrated and relatively low-cost for molecular diagnosis of lymphoma. The underpinning technology uses a high-resolution complementary metal-oxide-semiconductor (CMOS) image sensor to resolve target cells captured in a fluidic cartridge. Importantly, unlike digital microscopy, molecular specificity is obtained by staining cells with chromogen-labeled antibodies that generate holographic signatures rather than visual interpretation of cellular morphology. The assay occurs within disposable cassettes in which target cells are specifically captured and stained, thus minimizing the risk of exposure to healthcare providers or artifactual readouts from contaminants. Images containing up to 10,000 cells per field of view are detected by custom-developed deep learning (DL) algorithms and then reconstructed using either a cloud-based server within seconds or a local device within minutes. The end results include quantitative readouts of malignant cell number, cell size and differentiation between high- and low-grade subtypes based on specific marker expressions. We hypothesize that this approach would allow detection and triaging of lymphomas into aggressive and indolent subtypes, each with vastly different therapeutic approaches and urgency. To test this paradigm, we performed a prospective clinical trial with 40 patients referred for aspiration and biopsy of enlarged lymph nodes (lymphadenopathy) detected by whole-body imaging. This trial was designed as a validation study and conducted prior to future role-out to LMIC settings.

Results

Contrast-enhanced microholography for point-of-care diagnosis

We designed the CEM device as a portable, stand-alone digital microholography system (Fig. 1a, Fig. S1). The device is equipped with: 1) a CMOS image sensor with a light-

emitting diode for imaging; 2) a Raspberry Pi 3 module for cost-effective computing and image processing; 3) a wireless/Bluetooth unit for networking and 4) a touchpad screen for user-friendly operation. The CEM device is powered by either a corded power supply adapter or a lithium-ion battery pack for portable operation. Overall dimensions are 205 mm (L) x 120 mm (W) x 175 mm (H) and 1.4 kg in weight. The CEM assay for lymphoma diagnostics relies on immunostaining B-cells captured inside a disposable microfluidic cartridge (Fig. 1b). The cartridge's bottom glass surface is pre-functionalized with neutravidin to specifically capture B-cells — labeled with biotinylated CD19/CD20 antibodies — in a given sample (Fig. S2). This specific initial selection process measures captured B-cell counts and sizes. Enriched B-cells are then immunostained on-chip against kappa/lambda light chains or Ki67. While it is possible to interrogate many more molecular markers, we purposely limit them to the most relevant panel that still identifies B-cell lymphoma and distinguishes between aggressive and indolent lymphoma types (Fig. S3). To simplify analyses, we adapted deep learning technology using a convolutional neural network (Fig. 1c) trained on >5,000 holographic cellular lymphoma images (Fig. S4). The algorithm automatically detects captured B-cells directly from holograms without computationally intensive image reconstruction. Cell size and degree of staining are then calculated for each captured cell and displayed with colored circles.

Deep learning algorithm for cell detection

Fig. 2a shows a hologram image overlaid with pseudo-color circles showing the location, size and marker expression of each single cell. The images' field-of-view is about 5.7 mm x 4.3 mm, about 100 times larger than conventional microscope images using a 20x objective (N.A. = 0.4) yet image resolutions and sensitivities remain comparable (Figs. 2a and 2b). The deep learning algorithm identifies B-cells based on their holographic signatures while excluding non-cell objects (e.g. dust, debris, artifacts, noise, Fig. S5). The algorithm's detection accuracy matched conventional image reconstruction (Fig. 2c). After 250 epoch, the training accuracy reached 99% (Fig. 2d). With the deep learning algorithm, the computational time was five times faster than image reconstruction of the entire field-of-view. Using a cloud-connected central GPU server allowed reconstruction and analysis in less than 12 seconds for an average 10 MB PNG image; even when the local Raspberry Pi computer is used without GPU, analysis of 1,000 cells can be completed in 5 minutes (Fig. 2e). The computational time can be as short as 60 seconds for smaller cell counts (in the range of 200 cells). This is particularly important while operating the assay in rural areas where wireless internet connection is often slow or unavailable. Irrespective of the reconstruction method, both modes are enabled in the device, which switches between them automatically depending on internet availability.

Assay validation

We first validated the CEM assay using well-established lymphoma cell lines. Specifically, we used B-cell (Daudi and DB) and T-cell (Jurkat) cell lines to determine capture efficiency, size measurements, staining, sensitivity, specificity and reproducibility. B-cell lymphoma cells (Daudi and DB) exhibited a high capture efficiency of over 90% while the non-specific binding of Jurkat cells (T-cell) was below 5% (Fig. 3a). We observed a good correlation between expected and measured captured cell counts for mixtures of Daudi and Jurkat cells

with varying cell proportions (Pearson $r = 0.97$, $P = 0.0013$, Fig. 3b). We performed size calibration using different sizes of microspheres (3, 6, 8 and 16 μm) and again observed excellent correlation (Pearson $r = 0.99$, $P = 0.0020$, Fig. 3c). In order to enable immunostaining without the need for fluorescence, we tested different chromogenic substrates and identified one (ImmPACT VIP) that enabled the highest CEM contrast (Fig. 4a); it was used for all subsequent experiments. To validate CEM-based cellular profiling, we quantified expression of three target markers (kappa light chain, lambda light chain and Ki67) on three different cell lines. In the case of Daudi, kappa and Ki67 signals were high, while lambda and Ki67 signals were dominant in DB. As expected, the T cell line (Jurkat) only showed positive signal for Ki67 expression; these results are consistent with conventional flow cytometry analyses (Fig. 4b). To test the assay under more stringent environmental conditions, like those found in many LMIC, we lyophilized antibodies and tested different storage conditions (-20, 4, 25 and 37 °C). As is summarized in Fig. 4c, lyophilization showed good reproducibility with CEM variability being < 5%.

Clinical studies

Following the preclinical validation studies, we proceeded to patient-oriented testing. We designed a prospective trial with 40 patients referred for clinically indicated image-guided aspiration and biopsy of mass lesions suspicious for lymphoma. All patients gave informed consent for extra FNA passes. All pre-procedural images were reviewed, and co-axial needles were placed under computed tomography or ultrasound guidance (Fig. S6). Samples for routine clinical testing included multiple ($n = 4$ to 8) 21G passes for flow cytometry and cytopathology followed by 19G tissue cores for histopathology (all processed by the Pathology Department, Massachusetts General Hospital). Of the 4–8 FNA passes, one was processed for CEM analyses. For each CEM sample, total cell counts, B-cell counts, B-cell size and kappa, lambda or Ki67 positive B-cell counts were determined for integrated diagnoses (Figs. 5, S7, S8). The final automated CEM results were compared with clinical pathology and cytology data (Table S1).

Fig. 6a shows the decision tree for CEM-derived diagnoses of B-cell lymphoma and benign adenopathy. The decision tree reflects a simplified algorithm for lymphoma diagnosis in LMICs based on published literature[29], WHO guidelines[30,31] and our own practical experience in pathology at MGH. We first determined whether the collected samples had sufficient cell counts for CEM analyses. If fewer than 100 cells per marker were present, we deemed the sample non-diagnostic, which occurred in only 1 of the 40 specimens. It should be noted that this number was higher for clinical flow cytometry, which was non-diagnostic in 10/40 cases despite the higher number of FNA passes. Additionally, we set a secondary criterion that more than 10% cells are positive for at least one of three markers (kappa, lambda light chains and Ki67) to ensure the adequacy of a given test (Fig. S3).

A second sub-algorithm was used to determine if a given patient had malignant lymphoma or benign adenopathy. This was deciphered by B-cell population prevalence (> 20%) and clonality (kappa and lambda light chain expression, Fig. 6b). Based on prior work and historical controls, we defined lymphoid clonality as $(\kappa-\lambda)/(\kappa+\lambda)$ and characterized it as lymphoma when the ratio was greater than $+0.5 \pm 0.05$ (kappa dominant) or less than -0.5

± 0.05 (lambda dominant). For the 40 samples analyzed, CEM showed an accuracy of 95% (37/39, 1 non-diagnostic) in detecting malignant lymphoma (Fig. 6c and Table 1). The non-diagnostic case (#5) offered too few B-cell counts to accurately determine clonality. In comparison, review of official flow cytometry results, as interpreted by clinical hematopathologists, showed an accuracy of 87% (26/30, 10 non-diagnostic) with 3 false negatives and 1 false positive.

Furthermore, we used a combination of Ki67 staining and nuclear cell size measurements to determine whether each lymphoma case was aggressive/low grade. Among 24 lymphoma samples tested, CEM correctly identified 21 cases (2 false negative and 1 non-diagnostic). For the 21 lymphoma cases (Figs. 7a and b), aggressive lymphomas were defined as having > 45% Ki67+ cells (Fig. 7c) and/or having large fractions of large cell nuclei (> 15 μm; Fig. 7d). Using the above criteria, CEM correctly established the diagnosis of aggressive DLBCL in 6 of the 6 pathology-proven cases (Table 1). It should be noted that clinical flow cytometry was insensitive in detecting DLBCL, a finding also reported by others, likely due to the fragile nature of large lymphoma cells[32].

The low-grade lymphoma group (n = 15) comprised a mixture of follicular lymphoma (FL, n = 9), small B cell lymphoma (SBCL, n = 4) and mantle cell lymphoma (MCL, n = 2). CEM analyses determined two cases (#10 and #12, Table S1) to be aggressive based on high Ki67 levels alone. After incorporating clinical information (size of mass lesions, adenopathy or clinical history), all cases were correctly diagnosed (Table S2). CEM accurately diagnosed 16/16 cases of benign adenopathy while flow cytometry showed 1 false positive and 4 non-diagnostic cases.

Discussion

AIDS-related cancers, particularly lymphoma, are on the rise in subsaharan Africa due to improved survival via AIDS therapies[3–5]. Yet due to limited resources, lymphoma and other cancer diagnoses are often restricted to a few central hospitals and health centers. To enable clinical management-altering molecular diagnostics in the field, our efforts have focused on developing simple but effective tools that decentralize care. In the present project, we iteratively developed a stand-alone microholographic device and optimized it to analyze B-cell lymphoma. We integrated an advanced CMOS sensor, micro-computer, new on-chip staining techniques and an automated deep learning algorithm to establish a diagnosis that could be successfully rendered by a variety of health workers and not rely on highly sophisticated analytic techniques. A set of different biomarkers (CD19/20, Ki67, kappa and lambda light chains) were tested for lymphoma detection and classification. We show that the automated CEM method is surprisingly accurate and fast. Specifically, we obtained 91% sensitivity (21/23), 100% specificity (16/16) and 95% accuracy (37/39) for diagnosing lymphoma and 86% accuracy (18/21) in triaging lymphomas into aggressive and indolent types. No false positives were found for benign or disease-free samples, and only one sample was non-diagnostic due to low B-cell counts. In comparison, clinical flow cytometry showed 10 non-diagnostic cases with an accuracy of 87% (26/30) for diagnosing lymphoma. More importantly, flow cytometry was insensitive to distinguishing aggressive from indolent types. Given the limited number of molecular markers used here (CD19/20, Ki67, kappa and

lambda light chains; Fig. 5) compared to advanced work-up (CD19, CD20, CD3, CD5, CD10, CD15, CD30, kappa and lambda light chains, Ki67, Pax5, Alk1, cyclin D1), the diagnostic accuracy of CEM could also be improved. However, we decided not to pursue this at this time, as our primary objective was to validate the CEM method for deployment in sub-Saharan Africa, which is disproportionately impacted by aggressive lymphomas due to higher HIV incidence than in resource-rich regions such as North America[6,7]. This approach could triage lymphomas into those that require prompt chemotherapy and those that do not.

The current research was designed as a feasibility study to develop and validate point-of-care technology for lymphoma diagnosis. For robust field testing in a resource-limited setting, we expect improvement in the following areas prior to rolling out to LMIC testing: i) fewer steps for labeling and washing; ii) simplified assembly and maintenance of devices; iii) more secure data transmission and storage; iv) protection against potential contamination and v) prospective validation or adjustments of the current decision tree algorithm in larger patient datasets. We used well-established antibody conjugates coupled to peroxidases/phosphatases and chromogenic substrates such as ImmPACT VIP[33]. To simplify the various labeling and wash steps, we developed a disposable cartridge system to specifically capture and stain B-cells. Using these cartridges, antibodies can be lyophilized and stored at preferred temperatures for weeks without degradation; this is an important factor for field testing. Once rehydrated, cell samples can be introduced into the system. A new self-contained cartridge that can process a 1.5 ml reservoir and limit fluid handling and contamination is under development for field testing (Fig. S9). Safe handling is critical when dealing with specimens in HIV-endemic areas. Modular hardwares (imaging parts, microcomputers, power supplies) and open-source softwares reduce costs and maintenance.

The CEM technology is based on a free-standing platform for data acquisition, communication and result display(Fig. 1). We built the system from inexpensive components that add up to a fraction of the cost of the smartphone used in a previous system[11,28] while also containing a high-resolution CMOS image sensor. The current system components include the CMOS ($40), a touchpad screen display ($40), a Raspberry Pi computer with Bluetooth and WiFi ($40) and various small parts($30). Costs total ~ $180 per imaging system, one of the lowest-cost molecular diagnostic systems available even before economies of scale. While it is possible to perform holographic reconstruction directly on the Raspberry Pi computer, we opted for dual cloud-based integration to enable deep learning, speed up reconstruction and allow centralized input into the diagnostic output. The system allows diagnosis in < 1 minute through the cloud and < 10 minutes without internet access. By comparison, diagnostic turnaround times for various cancers can take months (median 160 days) in resource-constrained regions[34]. For the type of aggressive lymphoma for which CEM was designed, the Botswana Prospective Cancer Cohort identified a median time of four months (95% CI 2.1 to 11 months) between clinic visit and finalized diagnosis (unpublished data).

The current system is a first-generation platform that we intend to improve. Possible/planned upgrades/enhancements include implementing higher resolutions (or fields of view), multiplexing capabilities and adapting reagents to enable diagnosis of other malignancies such as Hodgkin's lymphoma[35] or carcinomas. These changes should improve detection

accuracies and allow for identifying sub-phenotypes. We also intend to extend the use of deep learning for rapid and accurate image analysis and diagnosis as we obtain more clinical data for training. In sum/Put simply, we expect our CEM technology will be highly beneficial in LMICs: at minimum, it will enable broad-based, decentralized patient triage (malignant vs. benign adenopathy; high-grade vs. low-grade lymphoma), and at best, CEM will provide detailed molecular analyses of lymphomas and other highly prevalent LMIC malignancies. Compared to flow cytometry and immunohistochemistry, the molecular diagnostics system reported here is significantly more cost-effective, operable by less-skilled health workers and well-suited for point-of-care settings, health clinics and rural areas.

Methods

CEM device

The integrated CEM imaging unit is equipped with a 1.4 A high-power 625-nm LED (Thorlabs) heat-sinked by a metal printed circuit board (PCB) and a custom machined aluminum holder. A 220-grit optical diffuser (DGUV10, Thorlabs) is positioned between the LED and a 50 μm pinhole (Thorlabs). Optical components are aligned by machined acrylonitrile butadiene styrene (ABS) mounts. Images are captured using a monochromatic 10 megapixel complementary-metal-oxide-semiconductor (CMOS) image sensor (On-Semiconductor) mounted on a USB 3.0 interface board (The Imaging Source). The pixel size is 2.2 μm and the field of view is $5.7 \times 4.3\ mm^2$. Image data are transferred from the camera to a Raspberry Pi 3.0 (Broadcom BCM2837 SoC) running Debian Linux. An integrated 7″ display (Raspberry PI Foundation) provides a real-time view of holographic data, and a touch-screen user interface captures and saves data. The touch-screen interface is written with the Kivy framework v1.10 running on a Python 2.7.9 interpreter. Images can be directly transferred via WiFi to a cloud-based GPU server for analysis. The unit is powered by a regulated 18 V, 60 W adapter (Meanwell) and runs continuously for approximately 2.5 hours when powered by an 3-cell, 4.2 V / 6.6 Ah Li+ battery pack. The device housing is 3d-printed (Formlabs), and the machined-aluminum door is fastened with 1/8 inch neodymium disc magnets (Grainger). The diffraction chamber is fabricated using opaque 1/8 inch acrylic sheets (laser ablation) and is light-proofed using flocking papers (Edmund Optics). The dimensions of the hardware unit are 205 mm (L) x 120 mm (W) x 175 mm (H) and the overall weight is 1.4 kg.

Cloud computing

A central server (GPX XS8-2460V3-4GPU) is equipped with two six-core Intel Xeon processors (E5-2609 v3 1.90GHz 15MB Cache), eight 16GB PC4-17000 2133MHz DDR4 and a graphic processing unit (GPU, NVIDIA Kepler K80). The K80 GPU has 4992 compute unified device architecture (CUDA) cores and 24 GB of GDDR5 memory. The operating system is based on Ubuntu Linux 14.04 LTS Server Edition 64-bit. The code is written in C++ and used vendor-provided modules (CUDA extensions, CUDA driver 7.0, CUFFT library). The imaging server periodically checks a dedicated folder in a cloud storage (Dropbox). When new image and image information is found, the server runs an image reconstruction. It then counts cells on the reconstructed frames. The reconstructed images and counting statistics are saved in a subfolder on Dropbox. When a Dropbox client

is synchronized, the image and data files can be accessed. All collected information is organized and stored in a secure web-based system (CSB Trials, Fig. S10) that supports multi-modal images in raw format. The developed in-house system is a multi-tier application that utilizes Ruby on Rails framework. All software is built using open-source modules. Data are stored in MySQL database; image conversions utilize dicomlib and ImageMagick.

Software architecture and deep learning

For detecting B-cells using deep learning, we implemented three modules that operate on a hologram image: maximally stable extremal regions (MSER) blob detection algorithm, faster non-maximum suppression algorithm and convolutional neural network (CNN). The MSER blob detection algorithm finds cell-like regions based on six parameters including region size, shape and intensities.

Once regions are proposed by the MSER algorithm, the bounding box coordinates are filtered by a non-maximum suppression algorithm with a maximum overlap threshold of 0.25. The remaining boundary box coordinates are mapped to a hologram input image, and each region is passed as input to the trained CNN for classification. The CNN was trained to classify a region as either containing one or more cells or containing no cells.

To train the CNN, the Adam optimization algorithm[36] was used to iteratively tune the weights in each CNN layer by calculating the CNN's loss at each iteration with respect to the ground-truth labels of each training example with the binary cross-entropy loss function. The training set was generated by using the MSER algorithm to detect regions from sample hologram images of cells, and each region was categorized as either "cell-like" or "non-cell" regions. The total size of the training set is 2,661 non-cell hologram regions and 2,509 cell-like hologram regions. The training set was split into 3,447 training samples and 1,723 validation samples. We used an Amazon Web Services p2.xlarge server with an Nvidia Kepler K80 GPU to run the training process over the entire training set for 250 epochs. All code is written using Python 3.6.1.

Diagnostic decision tool

Fig. S3 shows a decision tree used to analyze sample parameters. The B-cell population cut-off was obtained from a prior pilot study[28] while the clonality, Ki67 level, and size were defined by consulting literature[29–31] and standard operating procedures of flow cytometry at our institution. All parameters were then used prospectively in the current study. Specifically, the 20% CD19/20-positive B-cell population cut-off was based on a prior study[28] and this number assures that sufficient numbers of B-cells are present in a given sample to determine the clonality; by itself however, the cut-off does not have any discriminatory power. The threshold for clonality was set to 0.5 ± 0.05 (for kappa dominant) and -0.5 ± 0.05 (for lambda dominant) after reviewing published literature[29] and WHO guidelines[30,31]. To be classified as lymphoma, a given sample had to have a B-cell population over 20% of total cells and a monoclonal B-cell population (either kappa or lambda dominant). To pass quality assurance, we also defined a minimum number of cells (100 cells) for a given measurement and at least 10% of total cells had to be positive for kappa, lambda, or Ki67.

Reagents

Table S3 lists antibodies used in the study. For point-of-care operation, we further tested lyophilized antibodies. Antibodies (0.7 mg/mL, Ki67) were lyophilized using a freeze-dryer (FreezeMobile 25 EL, SP Scientific). The lyophilized antibodies were vacuum-sealed and then tested in different storage conditions (20, 4, 25 and 37 °C, Fig. 4c). The functionality of the lyophilized antibodies was tested and compared with fresh non-lyophilized antibodies. The glass substrates in flow cells were also lyophilized in the same conditions. Following rehydration with 60 μL of MilliQ water, cartridges and antibodies can be used without additional modifications.

Cell lines

Daudi (Burkitt's lymphoma), DB (germinal center B-cell like diffuse large B-cell lymphoma, DLBCL) and Jurkat (T-cell leukemia) cell lines were purchased from American Type Culture Collection (ATCC). All cell lines were maintained in RPMI-1640 medium supplemented with 10% heat-inactivated fetal bovine serum, 100 IU penicillin and 100 μg/mL streptomycin at 37 °C in a humidified atmosphere of 5% CO_2. Cell lines were routinely tested for mycoplasma contamination using MycoAlert^{TM} Mycoplasma Detection Kit (Lonza).

Optimization of staining assay

For assay optimization and validation, we performed a number of experiments in cell lines before moving to clinical samples (see below). We specifically tested i) different antibodies, ii) different substrates, iii) different staining conditions, iv) environmental influences and reagent stability and v) different flow chambers and reproducibility.

Fig. S11 summarizes the assay procedure. In general, harvested cells were fixed with 1x Lyse/Fix buffer (BD Biosciences) and incubated with biotinylated anti-human CD19 and CD20 antibodies (10 μg/mL). Cells were then permeabilized (0.005% saponin) and labeled with anti-human IgG kappa light chain, IgG lambda light chain or Ki67 antibodies (10 μg/mL) followed by HRP anti-rabbit IgG secondary antibody. Labeled cells were introduced into flow cells and incubated for 30 min. B-cells labeled with biotinylated anti-CD19/CD20 antibodies were captured on the neutravidin-coated surface of flow cells, and unbound cells were removed by washing at 40 mL/h for 1 mL. Captured cells were stained with Immpact VIP Peroxidase (HRP) substrate (Vector Labs) for 15 min. Three images per sample (pre-wash, post-wash and stained) were taken using the CEM device. Antibodies used are listed in Table S1. Assay buffer consisted of PBS supplemented with 2% BSA and 2% FBS. Samples were tested immediately or occasionally stored at −80°C in PBS (2% BSA) for future comparative use.

Flow cell cartridge

We designed flow cells using glass cover slips and sticker-type hybridization chambers to simplify fluid handling and staining. For field-testing, we developed flow cells with 1.5 ml reservoirs. The acrylic top cover was fabricated via laser ablation (Epilog 120W) of a clear 1.6 mm UV-resistant acrylic sheet. The silicone chamber was fabricated from a 0.8 mm high-temperature silicone sheet via laser ablation. The plastic base, including reservoir

chamber, was created by stereolithographic (SLA) printing with a clear photopolymer resin (Formlabs). A 25 x 25 mm glass coverslip (Gold Seal) is held in place by pressure fit between the silicone chamber and plastic base. The glass surface was first treated with 2% (3-aminopropyl)triethoxysilane (APTES, Sigma-Aldrich) for 30 min followed by 2.5% (v/v) glutaraldehyde in PBS (Sigma-Aldrich) for 2.5 h. A sticker-type hybridization chamber (9 mm diameter and 0.6 mm depth, Sigma-Aldrich) was used to confine the imaging area and the assay volume down to 60 μL. Finally, neutravidin (100 μg/mL) was permanently immobilized on the aldehyde-functionalized surface via reductive amination reaction using 4.5 mM sodium cyanoborohydride. The surface was washed extensively with PBS and then blocked with 1% BSA in PBS for 1 h. The flow cell cartridges with neutravidin were also lyophilized using the same protocol as antibodies. For CEM measurements, the flow cell was aligned and placed on the top of the image sensor. The gap distance between the flow cell and image sensor was approximately 0.5 ± 0.03 mm, which was estimated by our detection algorithm. For each sample, three flow cells were used for kappa, lambda, and Ki67 and were disposed after measurements.

Flow cytometry

In order to benchmark CEM measurements, we performed correlative flow cytometry using lymphoma cell lines. Half a million cells were prepared per marker using the same procedure as for CEM, except Alexa Fluor 488-conjugated secondary antibody was used instead of the HRP secondary antibody. Fluorescent signals were measured using BD LSRII Flow Cytometer (BD Biosciences) and normalized against isotope controls. Flow cytometry of clinical samples was performed by hospital Department of Pathology clinicians (see below and Table S2).

Patient study and clinical sample processing

We performed a prospective diagnostic study in which a FNA sample was obtained during clinically indicated image-guided FNA/biopsy of nodal mass lesions. This study and related materials (such as a consent form) were reviewed and approved by the Dana-Farber/Harvard Cancer Center Institutional Review Board. The investigators and other research staff ensured full study compliance with all relevant ethical regulations. Patients referred to the Division of Interventional Radiology at Massachusetts General Hospital because of clinically suspected new or recurrent lymphoma were enrolled following informed consent. Either ultrasound or computed tomography guidance was used to confirm correct needle position within a suspicious lymph node. Four to eight coaxial FNA passes yielded material for flow cytometry, cytopathology and CEM analysis. Additional core biopsies were obtained for conventional pathology work-up, which served as the gold standard alongside clinical information. For CEM analysis, FNA samples were fixed with 1x BD Phosflow Lyse/Fix buffer (BD Biosciences) and then processed as described for cell lines. CEM analyses were conducted blinded to conventional pathology and vice versa.

Data availability

The data supporting the findings of this study are available within the paper and its Supplementary Information. All data acquired in the course of this study are available from

the corresponding author upon reasonable request. Source data for the figures in this study are available in figshare with the identifier doi:10.6084/m9.figshare.6356867 (ref. 37).

Code availability

The codes for the detection of lymphoma cells are available at https://csb.mgh.harvard.edu/bme_software.

Supplementary Material

Refer to Web version on PubMed Central for supplementary material.

Acknowledgments

We would like to thank Jouha Min for assay optimization, Kaley Joyes for editing the manuscript and all members of MGH's Division of Interventional Radiology, Department of Pathology and Cancer Center who contributed to patient care. This work was supported in part by 5UH2CA202637 (R.W., B. Chabner), 4R00CA201248 (H.I.) and a grant from the V-Foundation for Cancer Research (R.W., C.M.C.). H.L. was supported in part by R21-CA205322, R01-HL113156 and MGH scholar fund. A.K. has been supported by the Mac Erlaine Scholarship from the Academic Radiology Research Trust, St. Vincents Radiology Group, Dublin, Ireland, and also by the Higher Degree Bursary from the Faculty of Radiologists at the Royal College of Surgeons in Ireland.

References and notes

1. Hsu CY, Jung SM, Chuang SS. Physician supply and demand in anatomical pathology in Taiwan. J Formos Med Assoc. 2011; 110:78–84. [PubMed: 21377061]
2. Nelson AM, Milner DA, Rebbeck TR, Iliyasu Y. Oncologic Care and Pathology Resources in Africa: Survey and Recommendations. J Clin Oncol. 2016; 34:20–26. [PubMed: 26578619]
3. Varmus H, Kumar HS. Addressing the growing international challenge of cancer: a multinational perspective. Sci Transl Med. 2013; 5:175cm2.
4. Livingston J. Cancer in the shadow of the AIDS epidemic in southern Africa. Oncologist. 2013; 18:783–786. [PubMed: 23882020]
5. Chabner B, Dryden-Petersen S, Efstathiou J. Cancer in Botswana: The Second Wave of AIDS in Sub-Saharan Africa. The Oncologist. 2013; 18:777–778. [PubMed: 23882018]
6. Naresh KN, Raphael M, Ayers L, Hurwitz N, Calbi V, Rogena E, Sayed S, Sherman O, Ibrahim HAH, Lazzi S, Mourmouras V, Rince P, Githanga J, Byakika B, Moshi E, Durosinmi M, Olasode BJ, Oluwasola OA, Akang EE, Akenòva Y, Adde M, Magrath I, Leoncini L. Lymphomas in sub-Saharan Africa – what can we learn and how can we help in improving diagnosis, managing patients and fostering translational research. Br J Haematol. 2011; 154:696–703. [PubMed: 21707579]
7. Carbone A, et al. Diagnosis and management of lymphomas and other cancers in HIV-infected patients. Nat Rev Clin Oncol. 2014; 11:223–238. [PubMed: 24614140]
8. Mwamba PM, et al. AIDS-Related Non-Hodgkin's Lymphoma in Sub-Saharan Africa: Current Status and Realities of Therapeutic Approach. Lymphoma. 2012; 2012:904367.
9. D'Ambrosio MV, et al. Point-of-care quantification of blood-borne filarial parasites with a mobile phone microscope. Sci Transl Med. 2015; 7:286re4.
10. Greenbaum A, et al. Wide-field computational imaging of pathology slides using lens-free on-chip microscopy. Sci Transl Med. 2014; 6:267ra175.
11. Im H, et al. Digital diffraction analysis enables low-cost molecular diagnostics on a smartphone. Proc Natl Acad Sci U S A. 2015; 112:5613–5618. [PubMed: 25870273]
12. Zheng G, Lee SA, Antebi Y, Elowitz MB, Yang C. The ePetri dish, an on-chip cell imaging platform based on subpixel perspective sweeping microscopy (SPSM). Proc Natl Acad Sci U S A. 2011; 108:16889–16894. [PubMed: 21969539]
13. Tapley A, et al. Mobile digital fluorescence microscopy for diagnosis of tuberculosis. J Clin Microbiol. 2013; 51:1774–1778. [PubMed: 23554191]

14. Laksanasopin T, et al. A smartphone dongle for diagnosis of infectious diseases at the point of care. Sci Transl Med. 2015; 7:273re1.
15. Yeo SJ, et al. Smartphone-Based Fluorescent Diagnostic System for Highly Pathogenic H5N1 Viruses. Theranostics. 2016; 6:231–242. [PubMed: 26877781]
16. Kanakasabapathy MK, et al. An automated smartphone-based diagnostic assay for point-of-care semen analysis. Sci Transl Med. 2017; 9:eaai7863. [PubMed: 28330865]
17. Priye A, et al. A smartphone-based diagnostic platform for rapid detection of Zika, chikungunya, and dengue viruses. Sci Rep. 2017; 7:44778. [PubMed: 28317856]
18. Kanakasabapathy MK, et al. Rapid, label-free CD4 testing using a smartphone compatible device. Lab Chip. 2017; 17:2910–2919. [PubMed: 28702612]
19. Ming K, et al. Integrated quantum dot barcode smartphone optical device for wireless multiplexed diagnosis of infected patients. ACS Nano. 2015; 9:3060–3074. [PubMed: 25661584]
20. Ko J, et al. Smartphone-enabled optofluidic exosome diagnostic for concussion recovery. Sci Rep. 2016; 6:31215. [PubMed: 27498963]
21. Meda BA, et al. Diagnosis and subclassification of primary and recurrent lymphoma. The usefulness and limitations of combined fine-needle aspiration cytomorphology and flow cytometry. Am J Clin Pathol. 2000; 113:688–699. [PubMed: 10800402]
22. Zeppa P, et al. Fine needle aspiration cytology and flow cytometry immunophenotyping of non-Hodgkin lymphoma: can we do better. Cytopathology. 2010; 21:300–310. [PubMed: 20132132]
23. Savage EC, Vanderheyden AD, Bell AM, Syrbu SI, Jensen CS. Independent diagnostic accuracy of flow cytometry obtained from fine-needle aspirates: a 10-year experience with 451 cases. Am J Clin Pathol. 2011; 135:304–309. [PubMed: 21228371]
24. Wei Q, et al. Plasmonics Enhanced Smartphone Fluorescence Microscopy. Sci Rep. 2017; 7:2124. [PubMed: 28522808]
25. Xu W, Jericho MH, Meinertzhagen IA, Kreuzer HJ. Digital in-line holography for biological applications. Proc Natl Acad Sci U S A. 2001; 98:11301–11305. [PubMed: 11572982]
26. Gurkan UA, et al. Miniaturized lensless imaging systems for cell and microorganism visualization in point-of-care testing. Biotechnol J. 2011; 6:138–149. [PubMed: 21298800]
27. Greenbaum A, et al. Imaging without lenses: achievements and remaining challenges of wide-field on-chip microscopy. Nat Methods. 2012; 9:889–895. [PubMed: 22936170]
28. Pathania D, et al. Holographic Assessment of Lymphoma Tissue (HALT) for Global Oncology Field Applications. Theranostics. 2016; 6:1603–1610. [PubMed: 27446494]
29. Matasar MJ, et al. Expert second-opinion pathology review of lymphoma in the era of the World Health Organization classification. Ann Oncol. 2012; 23:159–166. [PubMed: 21415238]
30. Swerdllow SH, Campo E, Harris NL. WHO classification of tumours of haematopoietic and lymphoid tissues. WHO Press; 2008.
31. Swerdlow SH, , et al. WHO classification of tumours of haematopoietic and lymphoid tissues (Revised 4th edition). Lyon: IARC Press; 2017.
32. Demurtas A, Stacchini A, Aliberti S, Chiusa L, Chiarle R, Novero D. Tissue flow cytometry immunophenotyping in the diagnosis and classification of non-Hodgkin's lymphomas: a retrospective evaluation of 1, 792 cases. Cytometry B Clin Cytom. 2013; 84:82. [PubMed: 23325563]
33. van der Loos CM. Chromogens in multiple immunohistochemical staining used for visual assessment and spectral imaging: the colorful future. J Histotechnol. 2010; 33:31–40.
34. Brown CA, et al. Predictors of Timely Access of Oncology Services and Advanced-Stage Cancer in an HIV-Endemic Setting. Oncologist. 2016; 21:731–738. [PubMed: 27053501]
35. Eichenauer DA, et al. Hodgkin's lymphoma: ESMO Clinical Practice Guidelines for diagnosis, treatment and follow-up. Ann Oncol. 2014; 25:iii70–75. [PubMed: 25185243]
36. Kingma Diederik P, Ba J. Adam: A Method for Stochastic Optimization. The International Conference on Learning Representations (ICLR); 2015;
37. Im H, , et al. Dataset for Design and clinical validation of a point-of-care device for the diagnosis of lymphoma via contrast-enhanced microholography and machine learning. figshare. 2018. http://dx.doi.org/10.6084/m9.figshare.6356867

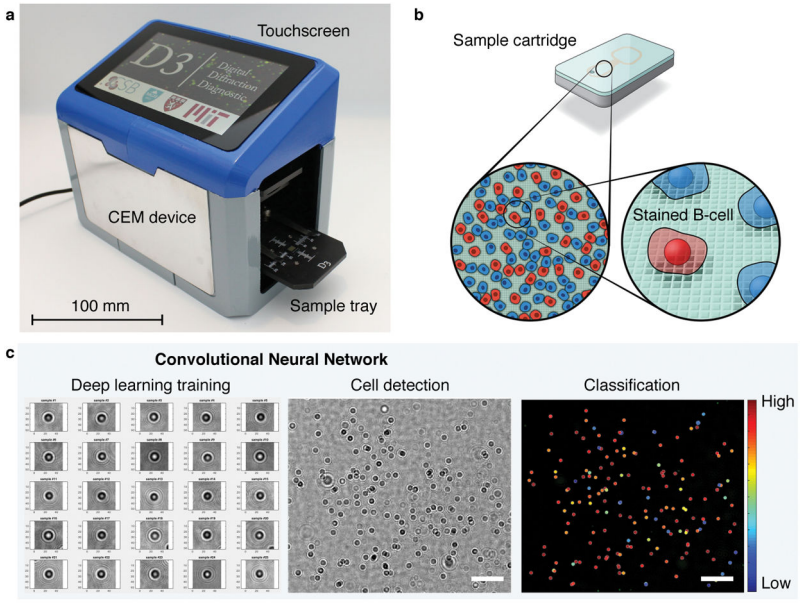

Fig. 1. Stand-alone CEM system

a, A photograph of the CEM device. The CEM device consists of an imaging component (an LED and a CMOS image sensor), microcomputer (Raspberry Pi 3 with wireless and bluetooth unit), 7-inch touch screen and sample tray. See Figure S1 for inner components. The case was fabricated by 3D printing. The overall size is 205 mm (L) x 120 mm (W) x 175 mm (H). **b**, CEM assay. Cells were labeled by antibodies and introduced into a disposable sample cartridge. B-cells were specifically captured on the bottom glass substrate and subsequently stained for kappa light chain, lambda light chain or Ki67. Hologram patterns of stained and unstained B-cells were imaged by the CEM device. **c**, A deep learning algorithm based on a convolutional neural network identified B-cells directly from holograms. Scale bars: 200 μm.

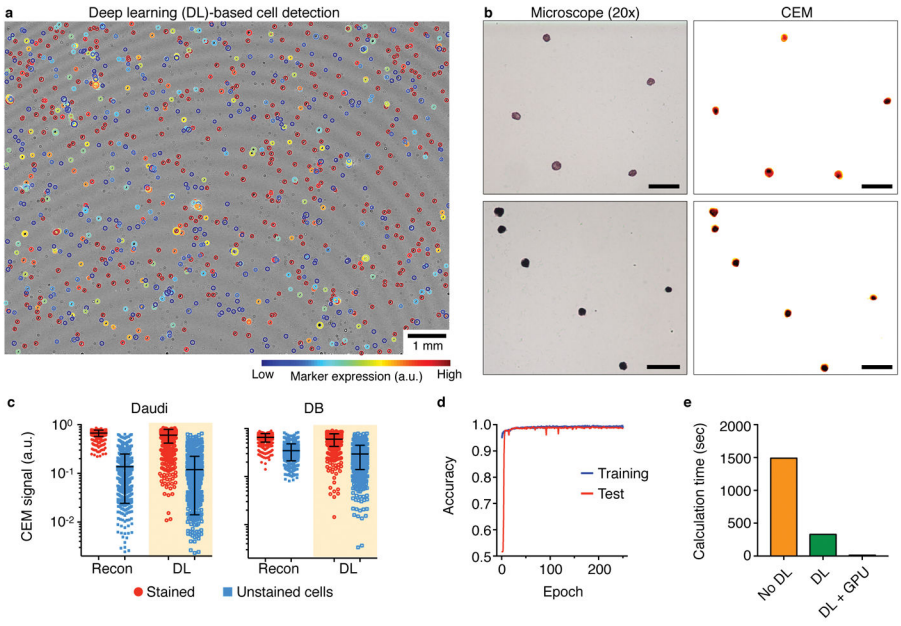

Fig. 2. B-cell detection using the deep learning algorithm

a, The deep learning algorithm identified B-cells and their locations. The images of found cells were further processed to measure the nuclear size and marker expression, depicted here by different-sized circles and their colors. The entire field of view (FOV) was ~ 25 mm^2, about 100 times bigger than the FOV of conventional bright-field microscope with a 20× objective. **b**, Comparison between bright-field microscope and CEM images. Stained color intensity correlated with marker expression. Scale bars: 50 μm. **c**, CEM signal comparison between the original image reconstruction method and the new deep learning algorithm. The error bars represent mean ± s.d. obtained from ~800 individual cells. **d**, The deep learning network was trained by >5,000 cellular and non-cellular hologram patterns and showed 99% accuracy in an independent test set. **e**, Using the deep learning algorithm, overall calculation time was 5 times shorter, and the entire image processing can be completed in 5 minutes. When using a central server with a graphic processing unit, the computation time is significantly improved and can be as short as 12 seconds.

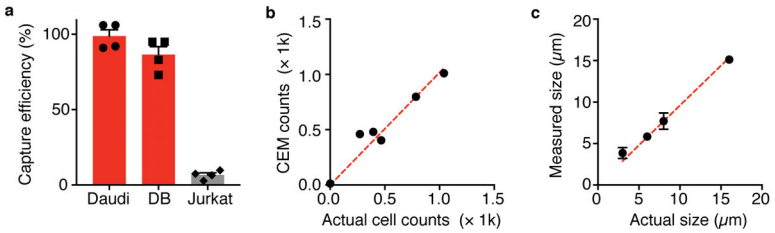

Fig. 3. B-cell capture and size measurement

a, B-cell capture efficiency was tested using two B-cell lymphoma (Daudi and DB) and T-cell leukemia (Jurkat) cell lines. For Daudi and DB, the device showed > 90% capture efficiency, while non-specific T-cell binding was < 5%. The bars represent mean ± s.d. from quadruplicate measurements. **b**, Correlation between expected and measured captured cell counts for Daudi and Jurkat cell mixtures with varying cell proportions (Pearson correlation coefficient $r = 0.97$; $P = 0.0013$). **c**, Size calibration with size-standard microspheres (3, 6, 8, and 16 μm) showing a linear correlation over the range tested (Pearson correlation coefficient $r = 0.998$; $P = 0.0020$). The dots represent mean ± s.d. from more than 10 measurements.

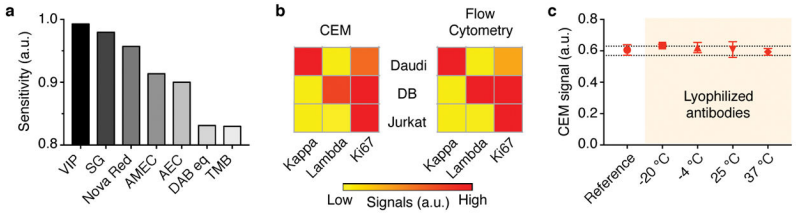

Fig. 4. Assay validation

a, Different chromogenic substrates were tested to reveal Ki67 in lymphoma cell lines. Among those tested, the ImmPACT VIP substrate showed the greatest contrast between stained and unstained control samples. **b**, The CEM measured marker expressions of kappa light chain, lambda light chain and Ki67 for three different cell lines (Daudi, DB and Jurkat) and compared to marker expressions measured by gold-standard flow cytometry. Note the congruency. **c**, Ki67 Antibodies were lyophilized and stored at different temperatures. After rehydration, the antibodies and the CEM assay showed good reproducibility with a standard variation of < 5%. At least 200 individual cells were analyzed for each condition and the data are displayed as mean ± s.d. Dashed lines indicate ± 5% of the mean value.

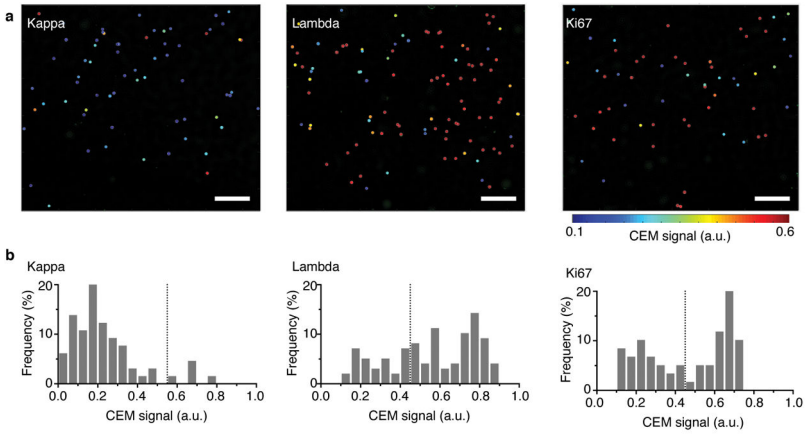

Fig. 5. CEM readouts for a single clinical sample (DLBCL example)

Each clinical sample obtained by fine-needle aspirates is tested for a number of parameters including total cell count, B-cell count (positive for CD19/20), B-cell counts positive for kappa light chain, lambda light chain and Ki67 and nuclear size. **a**, A representative example shows high lambda light chain, and Ki67 counts. **b**, Corresponding histogram graphs. An average of 77 B-cells were analyzed (59 – 98 B-cells) in each channel. Detailed numbers are summarized in Table S1. Scale bars: 250 μm.

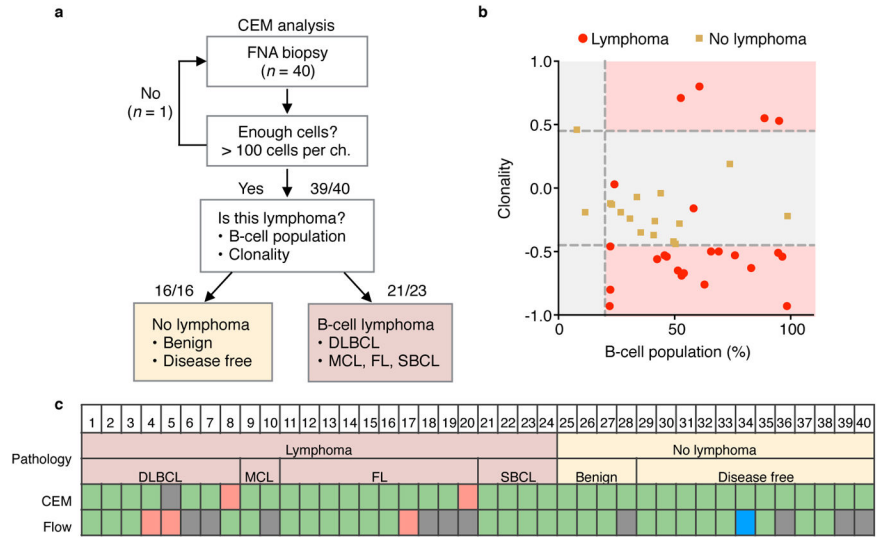

Fig. 6. Lymphoma diagnosis for 40 patients enrolled in a prospective trial

a, The CEM diagnostic algorithm for detecting B-cell lymphoma. **b**, 2D scatter plot of B-cell population vs clonality for lymphoma detection. Each dot represents a patient. **c**, Comparison of CEM diagnosis and flow cytometry. Green cells indicate correct diagnosis, blue cells are false positives, red means false negatives. Grey are non-diagnostic due to insufficient number of cells for diagnosis. DLBCL, diffuse large B-cell lymphoma; MCL, mantle cell lymphoma; FL, follicular lymphoma; SBCL, small B-cell lymphoma; DF, disease free.

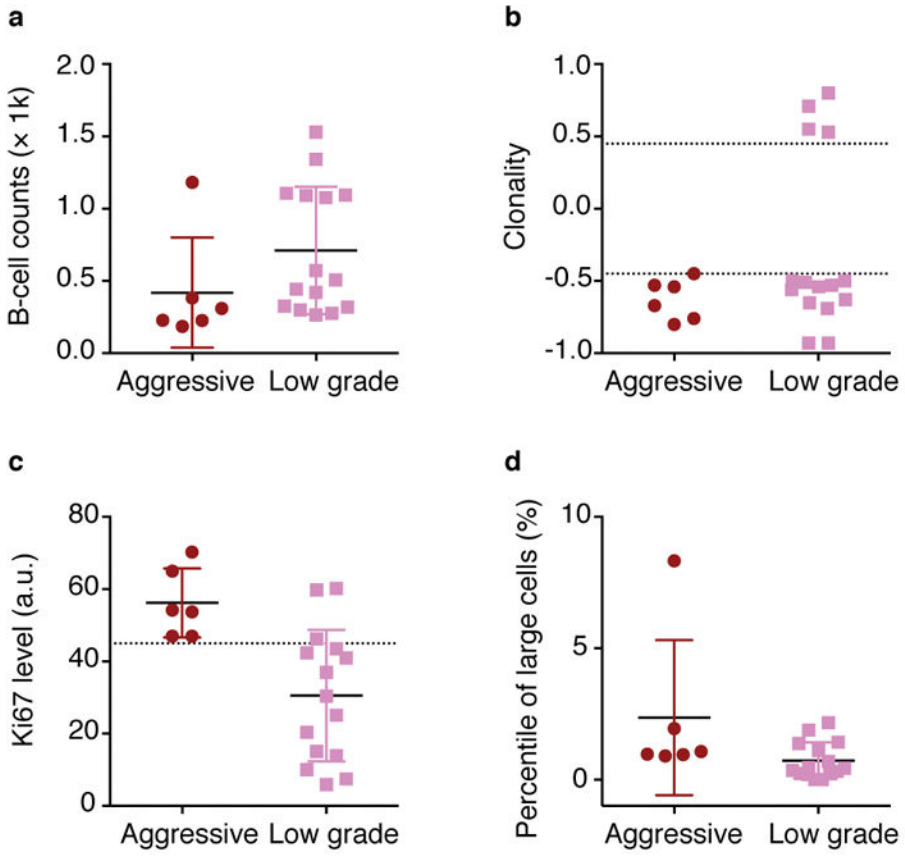

Fig. 7. Identifying high-risk, aggressive cases

a–d, B-cell counts (**a**), clonality (**b**), Ki67 level (**c**) and percentile of large cells (> 15 μm) (**d**) between aggressive (n = 6) and low-grade lymphoma cases (n = 15). The bars represent mean ± s.d.

Table 1

Comparison of detection sensitivity, specificity and accuracy

between CEM and flow cytometry for lymphoma diagnosis (left) and classification (right). TP, true positive; TN, true negative; FP, false positive; FN, false negative; ND, non-diagnostic. Sen, sensitivity; Spec, specificity; Acc, accuracy.

Lymphoma classification		
	CEM	**Flow**
TP	6	0
TN	12	11
FP	3	0
FN	0	5
ND	0	5
Total	21	21
Sen	100%	0%
Spec	80%	69%
Acc	86%	69%

Lymphoma diagnosis		
	CEM	**Flow**
TP	21	15
TN	16	11
FP	0	1
FN	2	3
ND	1	10
Total	40	40
Sen	91%	83%
Spec	100%	92%
Acc	95%	87%